

Chapter 1

Cooling and Trapping in a MOT

1.1 Chapter Outline

This chapter presents a description of the components of the experiment which are used to trap and cool atoms in a **mot!** (**mot!**). An outline of the hardware used to create both the 2D and 3D **mots!**s (**mots!**s) is presented in Section ???. Following this is a description of the μ Quans laser system, in Section ??, which generates the light used to cool and trap atoms. The hardware used to control the frequency and power of each **mot!** beam, as well as the required magnetic fields, is given in Section ???. Finally, this chapter concludes with a presentation of a measurement of the 3D **mot!** loading rate, which serves as a figure-of-merit for the performance of the **mot!** system.

1.2 The Navigator Vacuum Chamber

The vacuum chamber, along with the components mounted to it, make up the majority of the hardware used in the preliminary trapping and cooling stages of the experiment.

The chamber is made of 316L stainless steel which helps to minimise the influence of stray magnetic fields that could otherwise affect the performance of the **mot!**. The chamber contains 16 DN40 ConFlat ports arranged on the edges of three octagons, one in each cartesian coordinate plane. Six of these ports are used to provide optical access for the 3D **mot!**, and a further four are used to connect to the 2D **mot!** system, a gate valve, the NexTorr pump and to provide power to the in-vacuum 3D **mot!** coils. Two of the remaining ports are used to provide optical access for the imaging systems — a CCD camera and a photodiode — or a microwave horn, depending on the specific experiment. The last four ports are not used for additional optical access since their line of sight to the atoms is obscured by the **mot!** coils. Two DN63 ports lie along one axis, which is conventionally taken to be the x axis. These ports are used to mount the optics for driving Raman transitions and as such, defines the axis along which the atom interferometer is sensitive to accelerations¹.

A diagram of the vacuum chamber and the main **mot!** components is shown in Figure ???. The chamber is pumped down to a pressure of around 5×10^{-10} mbar using a NexTorr D100-5 pump. This is a composite system consisting of **neg!** (**neg!**) and an ion pump. The **neg!** is a porous sintered zirconium (St 172) element, which reacts with chemicals such as hydrogen, water, nitrogen, oxygen and hydrocarbons. Most of these were removed during the initial baking and roughing pump stages. Under **uhv!** (**uhv!**) conditions, the largest contributor to the pressure is hydrogen which the **neg!** can pump at a speed of 100 l s^{-1} . Any species that are not absorbed by the **neg!**, in particular Rubidium, are pumped by the 5 l s^{-1} ion pump.

¹For more information about the Raman optical system, refer to Section ??

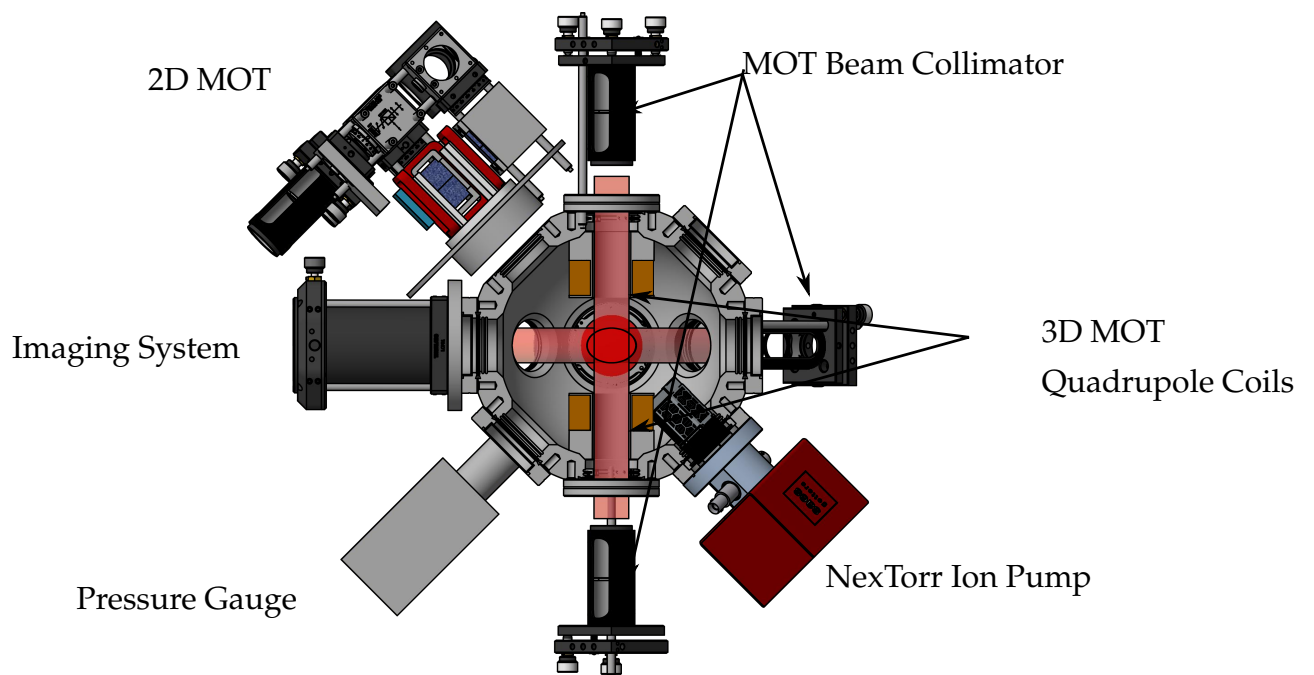


Figure 1.1: A diagram of the main components on the vacuum chamber used for the **mot!** systems. Rubidium atoms are dispensed and loaded into the 2D **mot!** before being pushed into the main chamber and collected in the 3D **mot!**. A set of 6 beam collimators provide the light necessary to slow and cool atoms, which are trapped using the spherical quadrupole field generated by the illustrated coils. Not shown are additional bias coils along each **mot!** beam axis to null stray fields at the centre of the chamber.

1.2.1 The 2D MOT system

Initially, atoms were loaded into the 3D **mot!** from a background vapour. Whilst this was a relatively simple scheme, a very high partial pressure of Rubidium is required to achieve a fast loading rate (see Section ??). However, this was undesirable from the point of view of the atom interferometer, as it would result in a poor fringe contrast due to collisions with background atoms and a worse signal to noise ratio, i.e. the ratio of the number of atoms in the interferometer to the total number of detected atoms. Replacing the source of atoms for the 3D **mot!** with a side-arm to function as a 2D **mot!** [Dieckmann1998] satisfied the two requirements of a fast loading rate and low base pressure in the main chamber.

A diagram of the light and magnetic fields required to produce a 2D **mot!** is presented in Figure ?. It is similar to the 3D **mot!**, with the main exception being that only 4 beams are used to cool the atoms along 2 orthogonal axes. In addition to this, its design is focused towards the production of a large flux of cold atoms which can be subsequently loaded into a 3D **mot!**. For instance, the beams used to cool the atoms are collimated to a large waist size and the coils are designed to give a cylindrical quadrupole field with a line of zero magnetic field along the axis of symmetry. Along this axis, the atoms are free to move which results in an atomic beam. To improve the collimation of this atomic beam, a larger radial field gradient than usually used in a 3D **mot!** system is used to increase the radial confinement of atoms. In addition, a pinhole is placed at the exit of the cell, so that atoms with a high radial velocity component will miss the aperture. This pinhole also greatly reduces the conductance between the 2D **mot!** cell and the main chamber, which means that a comparatively high background pressure (hence, loading rate) can be maintained in the 2D **mot!** cell, without greatly increasing the pressure in the main chamber. The pinhole is drilled into a silicon plate, which is used to partially reflect a beam that propagates along the central axis. This

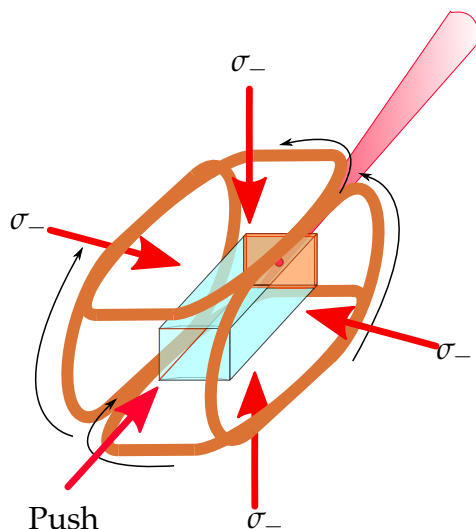
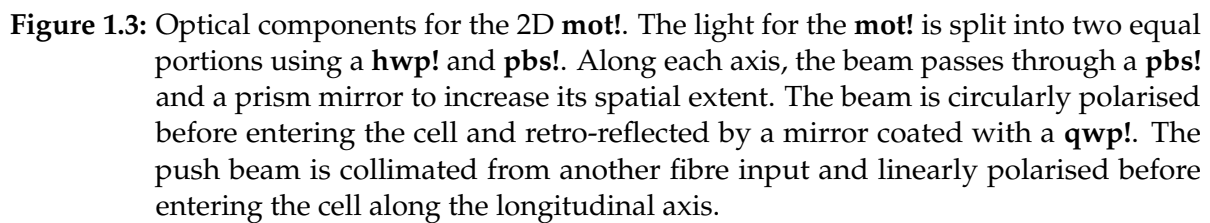


Figure 1.2: Schematic diagram for the 2D **mot**!. **rb87**! atoms are trapped and cooled along the 2 axes orthogonal to the long axis of the source cell. The arrows indicate the direction of the current through each coil, so that each circularly polarised beam drives σ_- transitions for an atom moving in the opposite direction. A linearly polarised push beam propagates along the remaining axis and is partially reflected by the silicon wafer at the opposite end. This provides a small amount of axial cooling and the imbalance of radiation pressure pushes atoms out of the cell. The pinhole at the other end prevents atoms with a high transverse velocity from leaving the cell.

creates an unbalanced molasses that cools atoms with a large axial velocity and due to the differing radiation pressure, pushes atoms out through the pinhole. By slowing a larger proportion of atoms to within the capture velocity of the 3D **mot**! and not solely relying on diffusion of the atoms, this configuration, often referred to as a 2D **mot**!, loads a 3D **mot**! faster than the 4-beam counterpart.

A schematic of the optical components for the 2D **mot**! is presented in Figure ???. The cooling light originates from a single fibre, which is collimated using two aspheric lenses to a beam waist of 9.5 mm and linearly polarised before being evenly split into two beams using a **hwp**! (**hwp**!), one for each cooling axis. Each beam passes through a beam-splitter and a prism mirror, to increase the volume covered by the 2D **mot**! beams and is circularly polarised by a pair of **qwp**! (**qwp**!) before entering the **ar**! (**ar**!) coated glass cell. On the opposing side of the cell, a 25 mm × 35 mm retro-reflecting mirror is used to provide the counter-propagating **mot**! beam. This is coated with a



layer of quartz to form a **qwp**!, so that the reflected beam has the required polarisation for cooling atoms along that axis. The push beam is created using a second fibre input and a fixed collimator to give a beam waist of 1.5 mm. This is mounted onto a 1 in kinematic mount so that the alignment of the push beam with respect to the 0.7 mm pinhole at the other end of the cell can be optimised. A linear polariser is placed here to reduce the effect of polarisation drift on the axial cooling of the 2D **mot**!. The cell, manufactured by ColdQuanta, has dimensions of 30 mm \times 30 mm \times 44 mm and is specifically designed for creating a 2D **mot**! and contains two rubidium dispensers composed of rubidium chromate (RbCrO_4) and a reducing agent. These were activated by passing a large current through them to remove a thin oxidation layer. To produce rubidium, a current is passed through the dispenser to trigger an electro-chemical reduction reaction. The reducing agent also acts to sorb the unwanted products, so that they do not contaminate the cell and only rubidium evaporates from the dispenser.

The cylindrical quadrupole field is generated by a set of coils that are manufactured by ColdQuanta. Their geometry is such that the axis of zero magnetic field coincides with the central longitudinal axis of the source cell. These produce a radial field gradient per current of $20 \text{ G cm}^{-1} \text{ A}^{-1}$. A simulation of the field gradient along each axis, along with the magnetic field in each plane of symmetry is shown in Figure ??, which indicates that the field gradient is very uniform across the centre of the cell. In addition to this, each **mot!** axis has a separately controlled pair of coils in a Helmholtz configuration to provide a bias field that cancels nulls the field along the 2D **mot!** axis. These coils are made of 20 turns of wire that has a core diameter of 1 mm and produces a field per current of $z \text{ G A}^{-1}$.

1.2.2 The 3D MOT system

The main chamber contains the apparatus that is used to make a 3D **mot!**. A diagram of the optical and magnetic fields used to create this **mot!** is presented in Figure ?. Each **mot!** beam is created using a collimator as shown in Figure ?. Light enters through a **pm!** (**pm!**) fibre using an FC/APC connector and is collimated using a 75 mm focal length lens to give a collimated beam with a waist size of 7.5 mm. At the output of each collimator is a **qwp!**, with its slow axis oriented at a 45° angle to the fast or slow axis of the fibre, depending on the particular collimator, to produce either left- or right-handed circularly polarised light. The **mot!** beams are oriented so that their intersection is at the centre of origin of a cartesian coordinate system. Since the **mot!** forms at the position where the magnetic field is zero, this system is set up so that beams overlap at the centre of the chamber, which is equidistant from each **mot!** coil. The **mot!** beams along the axial direction of the quadrupole field (conventionally referred to as the \vec{z} direction) are orthogonally polarised to the others along the \vec{x} and \vec{y} directions. This takes into account of the different direction of the magnetic field

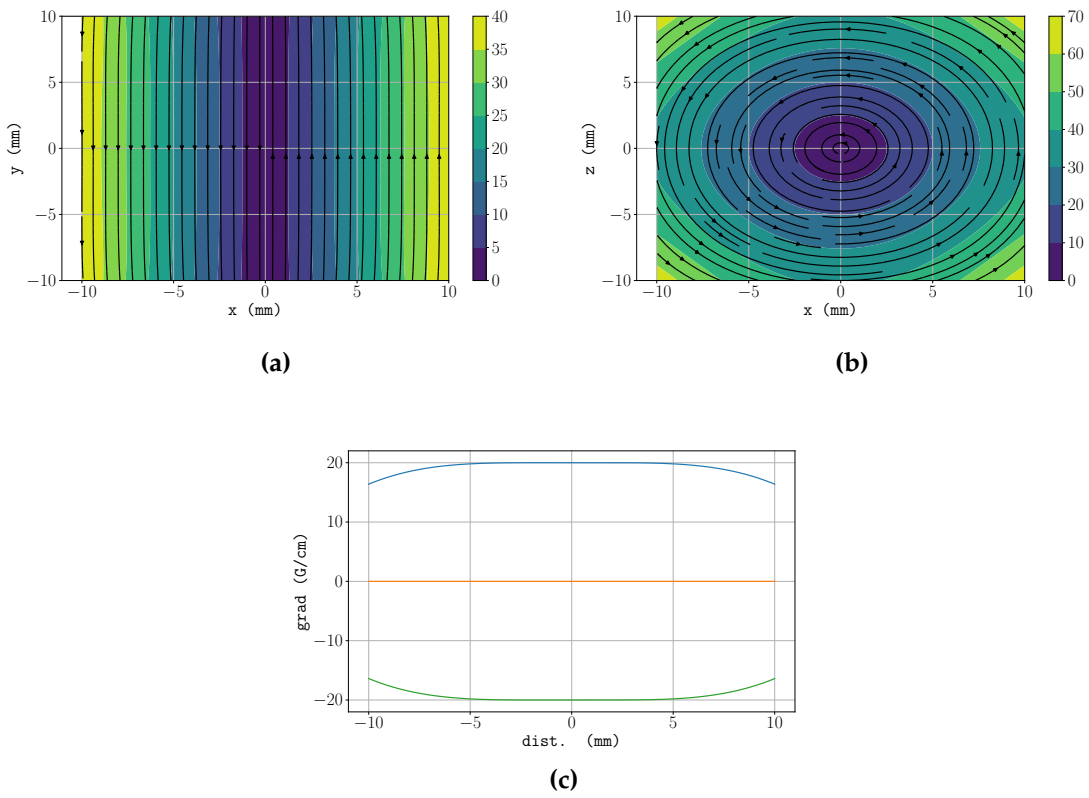


Figure 1.4: Simulated field and field gradients for the 2D **mot!** quadrupole coils. In this coordinate system, the 2D **mot!** cools and traps atoms in the \vec{x} and \vec{z} directions. The simulation was performed using a nominal current of 1 A, which corresponds to a current density in each coil of 7.78 A mm^{-2} . The magnitude of the magnetic field (in units of G) and its direction in the axial and radial planes of symmetry are shown in (a) and (b), respectively. (c) shows the field gradient components $\partial_x B_x$ (blue), $\partial_y B_y$ (orange) and $\partial_z B_z$ (green) along their corresponding axes.

gradient along each axis (see below), so that the polarisation of each **mot!** beam is such that an atom moving away from the centre of the trap is slowed and optically pumped into a state which feels a conservative potential.

Spherical quadrupole magnetic field

The magnetic field for the 3D **mot!** is created by a pair of coils in an anti-Helmholtz configuration. Along the axis of symmetry, the magnetic field from a current-carrying loop is given by the Biot-Savart law. **Some description of the spherical quadrupole field.** Each coil consists of rectangular wire coated in a 35 μm thick layer of Pyre-M.L, a UHV-compatible polyamide which provides a layer of insulation between each loop. The wire has a cross-section of dimensions 1.1 mm \times 1.1 mm, with 20 axial loops and 12 radial loops. The inner diameter of the coil is 25.4 mm, to allow for optical access of the \bar{z} -axis **mot!** beams, and the maximum diameter is 59.2mm – small enough that the coil could be inserted into the chamber through the DN63 CF ports. The coils are mounted to the chamber using groove grabbers which clamp into grooves inside the wall of the DN40 ports. The formers are designed to maximise the surface area between them and the chamber, which in turn aims to maximise the rate at which heat is dissipated from the coils. Once mounted, the distance between the innermost loops is 70 mm. Figure ?? shows the magnetic field, measured using a Hall probe, along the axis of symmetry for each of the coils with a current of 2.53 A. In addition to this, the field and corresponding axial field gradient when the coils are separated by 70 mm is shown in Figure ?. This is in close agreement with the value expected from simulating the field produced by the coils - the magnetic field in the axial and radial planes of symmetry and shown in Figure ?? and Figure ??, respectively.

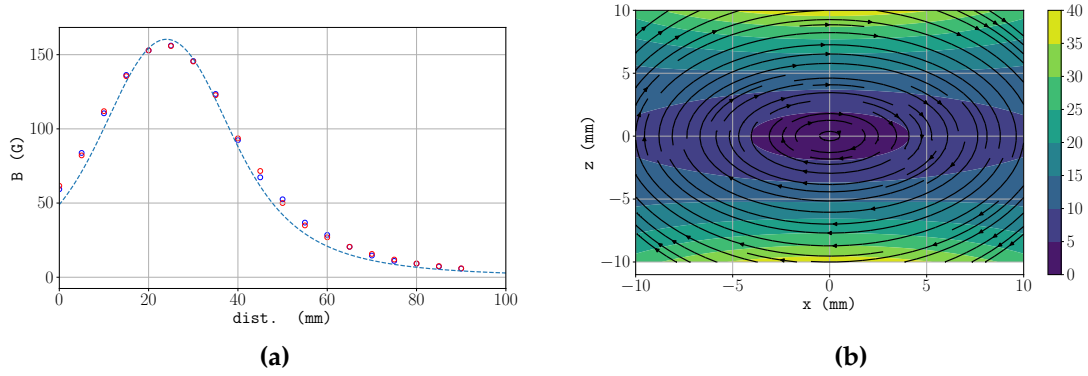


Figure 1.5: Measured magnetic field and field gradient for the 3D **mot!** coils. (a) shows the axial magnetic field for the two coils as measured using a Hall probe. The dashed line is the axial field as calculated from the simulation shown in Figure ??.

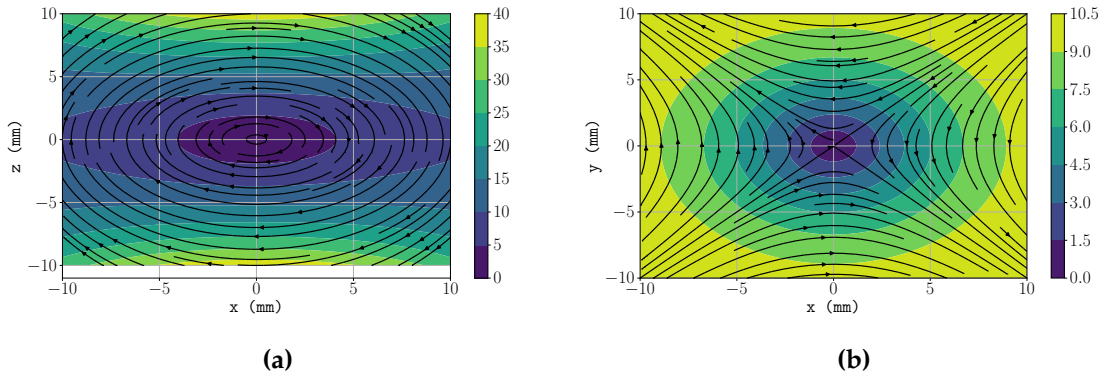


Figure 1.6: Simulated magnetic field for the 3D **mot!** quadrupole coils. In this coordinate system, the axial direction is defined as the \hat{z} axis. The simulation was performed using a nominal current of 2.53 A, which corresponds to a current density in each coil of 1.33 A mm^{-2} . The magnitude of the magnetic field (in units of G) and its direction in the axial and radial planes of symmetry are shown in (a) and (b), respectively.

Axis	a (mm)	r_i (mm)	r_o (mm)
\vec{x}	88	105	115
\vec{y}	132	178	188
\vec{z}	116	123	133

Table 1.1: Table of parameters for each 3D **mot**! bias coil. a denotes the axial separation between each coil, r_i and r_o are the inner and outer radii. Each coil was wound to give 50 loops (5 axial and 10 radial turns).

Bias Coils

Three orthogonally arranged pairs of Helmholtz coils are used during the experiment to null the magnetic field at the centre of the chamber. This is required for strong sub-Doppler cooling of the atom cloud in an optical molasses where the presence of a magnetic field reduces the cooling efficiency [Walhout1992]. These coils are also used in subsequent stages of the experiment to provide a bias field along the appropriate axes during state preparation, interferometry and state detection. Each coil was wound using 1 mm thick wire and consisted of 5 axial and 10 radial turns. For a pair of coils in Helmholtz configuration, the magnetic field gradient at the centre is minimised when the axial separation a is equal to the coil radius r , but the geometry of the vacuum chamber meant that it was not possible to satisfy this condition. The radii and axial separations of each coil pair is presented in Table ??.

1.2.3 CCD Imaging

The characterisation of the **mot**! stage of the experiment was achieved using a CCD camera to spatially resolve the atom cloud by detecting light emitted from the atoms during resonance fluorescence. Measuring the spatial distribution of atoms is useful, for example in estimating the temperature of the cloud by measuring the rate of thermal expansion. Figure ?? shows a diagram of the apparatus used for imaging.

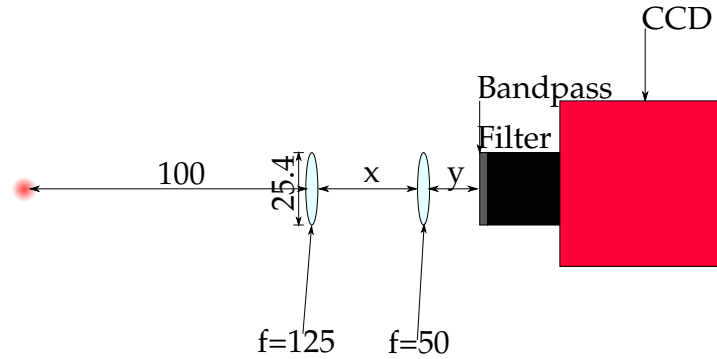


Figure 1.7: Optical setup for CCD imaging. Two lenses are used to magnify the image of the atom cloud on the CCD. A bandpass filter is placed in front of the sensor to block out background light at wavelengths other than 780 nm. All lengths are given in millimetres.

A pair of 125 mm and 50 mm focal length lenses are used to image the cloud onto a Pike F505-B CCD camera, which has a maximum resolution of 2452×2054 pixels. The pixel size in the object plane was measured by placing a ruler in that plane, giving a calibration factor of 5.1 pixel/mm. A bandpass filter is placed between the lens and the CCD which transmits 780 nm light at an efficiency of 60% and blocks background light at other wavelengths.

As well as being used to gain information about the spatial distribution of atoms, the CCD camera can be used to make an estimate of the number of atoms N_a by measuring the amount of light emitted during resonance fluorescence. However, it is worth noting that this is not a reliable method for determining the number of atoms in a **mot!**. Typically, the density of atoms is such that the incident light is significantly absorbed by the outer atoms, resulting in a weaker intensity close to the centre. Consequently, the assumption of a constant scattering rate per atom is not valid and leads to an under-estimate of the atom number. A more accurate measurement can be performed by measuring the amount of light absorbed by the atoms, which accounts for the optical thickness of the **mot!**. For the purposes of this experiment, it was sufficient to use the fluorescence imaging to provide a rough estimate of the number of atoms in the **mot!**. In subsequent stages of the experiment, where the atom number density

was much lower, a photodiode with greater sensitivity than the CCD was used to measure the number of atoms. Details on this setup can be found in Section ???. Under the assumption that the power radiated per atom is constant, the power incident on the CCD P_{ccd} can be related to the scattering rate per atom as follows

$$P_{\text{ccd}} = \frac{\Omega}{4\pi} t R_{\text{sc}} \hbar \omega N_a \quad (1.1)$$

where $\Omega/4\pi = \text{xsr}$ is the fractional solid angle subtended by the imaging optics, t is the transmission of the bandpass filter, R_{sc} is the scattering rate as previously defined in equation (??) and $\hbar \omega = 1.6 \text{ eV}$ is the emitted photon energy. This incident power is then related to the integrated number of pixel counts C_{int} by

$$C_{\text{int}} = \alpha \tau_{\text{exp}} \eta P_{\text{ccd}} \quad (1.2)$$

where τ_{exp} is the exposure time, $\eta = 0.14$ is the quantum efficiency of the CCD and α is a scaling factor that relates the total charge collected to the total number of pixel counts. By varying the exposure time used to image a collimated beam with a total power of $0.17 \mu\text{W}$, the total number of counts recorded by the camera as a function of exposure time is plotted in Figure ??. This gives a count scaling factor of $\alpha = 2.2 \times 10^5 \text{ counts } \mu\text{s}^{-1} \mu\text{W}^{-1}$.

1.3 Generating MOT light

All the **mot!** light in this experiment was generated by the μQuans laser [[muquansWebPage](#)]. μQuans is a French laser company that is a spin-off from the Institut d'Optique and Observatoire de Paris. A schematic of this laser system is shown in Figure ??. All of the light is fibre-coupled to minimise the number of free-space optical components and

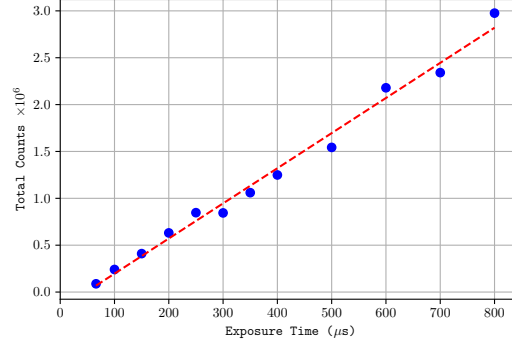


Figure 1.8: Integrated pixel counts as a function of CCD exposure time for an incident optical power of $0.17 \mu\text{W}$. The dashed line indicates a linear regression which gives a scaling factor of $\alpha = 2.2 \times 10^5 \text{ counts } \mu\text{s}^{-1} \mu\text{W}^{-1}$.

to make the system more stable in the presence of vibrations and small temperature variations. The μQuans laser is comprised of four 1560 nm **ecdl**s (ecdl)s which are frequency-doubled to produce light at 780 nm. The first of these acts as a master laser which is locked to the $F = 3 \rightarrow F' = 3, 4$ crossover point in **rb85** (rb85!) and serves as an absolute frequency reference. The other three slave lasers are used for output. The first one is used to provide light for cooling, as well as repump light by modulating the phase of this laser using an **eom** (eom!). The other two make up a pair of lasers for driving Raman transitions. One laser is frequency-offset locked to the master and the other is phase-locked to the first, to ensure that the relative phase between the two lasers is constant. It should be noted that this Raman laser was not used in this experiment, so will not be discussed in further detail. Each of these slave lasers is amplified in an **edfa** (edfa!) before being frequency doubled in a **ppln** (ppln!) and passed through an **aom** (aom!) which is used to control the output power during the experiment.

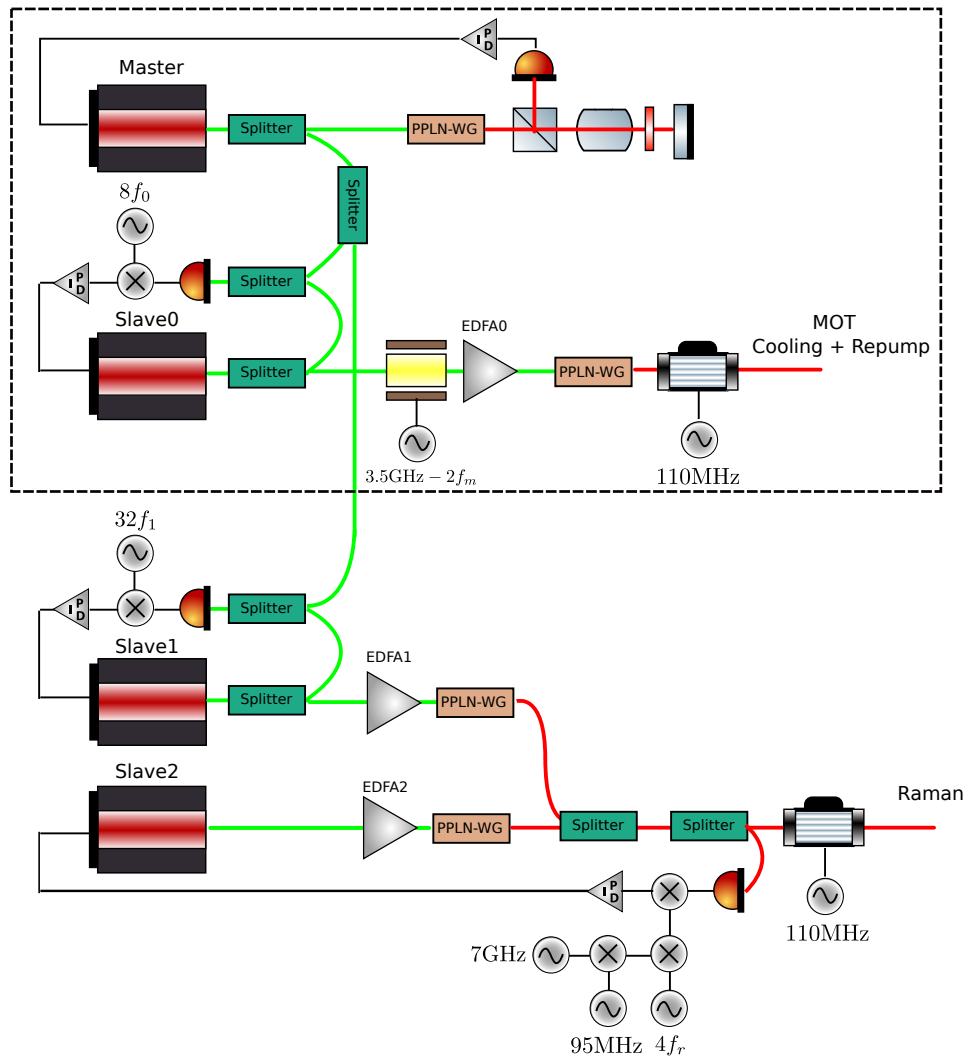


Figure 1.9: Schematic of the μ Quans laser system. Each output laser is derived from a 1560 nm **ecd1**! (shown in green) which is amplified using an **edfa**! and then frequency-doubled to 780 nm using a **ppln**! crystal. A master laser is locked to the 3,4 crossover in **rb85**! and the output lasers are offset-locked to their corresponding frequencies. The dashed region indicates the components used for generating light for the **mots**!, which was the only function of this laser for this experiment.

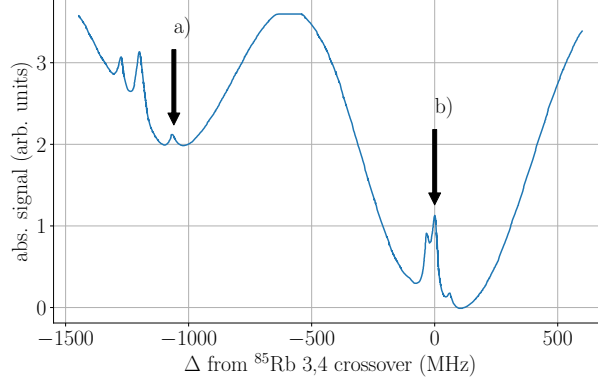


Figure 1.10: Saturated absorption spectroscopy using the Rubidium vapour cell in the μ Quans laser. The absorption features indicated are *a*: the $F = 2 \rightarrow F' = 3$ transition in **rb87!** and *b*: the crossover resonance between the $F = 3 \rightarrow F' = 3$ and $F = 3 \rightarrow F' = 4$ transitions in **rb85!** which is used to lock the frequency of the master laser.

1.3.1 Absolute Frequency Reference

The master laser is used to provide an absolute frequency to which the slave lasers are offset-locked. The frequency of the master is obtained using saturated absorption spectroscopy inside a Rubidium vapour cell. The sub-Doppler features in this spectrum are insensitive to temperature changes, and under sufficiently weak laser power have linewidths close to the natural linewidth of Rubidium ($\Gamma \sim 2\pi \times 6\text{MHz}$). Figure ?? shows the saturated absorption spectrum using the μ Quans master laser. This is obtained by fine adjustment of the temperature of the master **ecd!** (**ecd!**). The master laser is set to lock to the crossover resonance between the $F = 3 \rightarrow F' = 3$ and $F = 3 \rightarrow F' = 4$ transitions in **rb85!** (indicated as *b*), which is the strongest feature in the spectrum. This absorption feature is around 1.1 GHz below the cooling transition in **rb87!** (indicated as *a*). The frequency of the laser is modulated to produce a signal which is proportional to the difference from the lock point. This is done by modulating the current to the master **ecd!**. The error signal shown in Figure ?? is obtained by demodulating the absorption signal using a lock-in amplifier. In addition

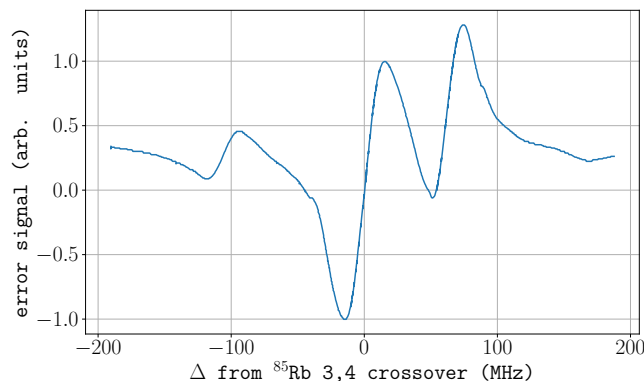


Figure 1.11: Error signal obtained by modulating the laser current. Close to the lock point, the signal is approximately linear. This signal is used in a feed-back loop to correct for frequency changes of the master laser.

to proportional feed-back from the error signal, the servo that controls the master laser frequency also contains an integrator to compensate for long-term drifts arising from temperature variations, for instance.

1.3.2 Cooling and Repump Light

The cooling light is generated by the first of the slave lasers. This is frequency-offset locked to the master by comparing their beat frequency to a local oscillator. The reference frequency is generated by a **dds!** (**dds!**) and is scaled up by a factor of 8. A plot of the error signal used to lock this offset frequency is shown in Figure ??.

Light for driving the $F = 1 \rightarrow F' = 2$ repump transition is generated using an **eom!** that modulates the phase of the cooling laser to produce sidebands separated by integer multiples of the modulation frequency f_m . If the amplitude of the modulation frequency is small, only the first positive and negative sidebands are present. The modulation frequency is generated by another **dds!**, so that the frequency of the cooling and repump light can be ramped during the experiment independently (see Section ??). This is amplified, doubled and subtracted from a 3.5 GHz reference signal

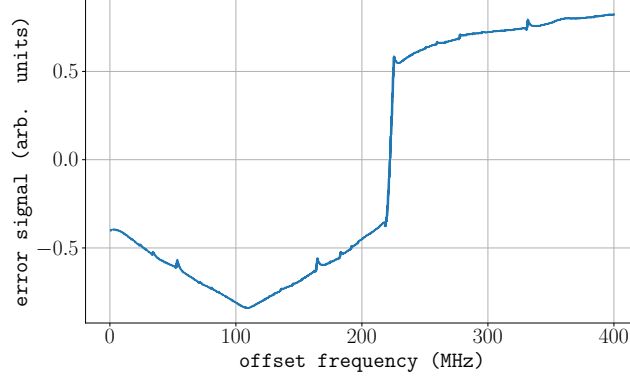


Figure 1.12: Error signal for the μ Quans cooling laser, plotted as a frequency difference from the start of the scan. This is obtained by comparing the beat frequency between the master and slave lasers to a reference frequency generated by a **dds!**. A servo loop feeds-back onto the frequency of the slave laser to keep this difference close to zero.

so that the positive frequency sideband is approximately 6.6 GHz above that of the cooling light, to address the repump transition. The power of this modulation signal can be externally controlled using a **vca!** (**vca!**) to control the ratio of repump power to cooling power. An RF switch is also used to switch the repump light on or off.

The total output power is controlled using an **aom!** that has a fixed modulation frequency of 110 MHz. Similarly to the repump **eom!**, a **vca!** is used to control the amplitude of this modulation to control the output power, as well as an RF switch to block the output.

1.3.3 Real-Time Control

During the experiment, it is necessary to vary the frequency and power of both the cooling and repump light. As mentioned above, the power is controlled using analogue and digital signals to the RF sources for the output **aom!** and **eom!**, respectively. Control of their frequency is achieved using the **dds!** that controls the corresponding reference frequency. In addition to updating the frequency of the slave or its sideband,

the **dds!** can be programmed to ramp the frequency on a chosen output for a given duration and ramp rate. This is done during the experiment by sending serial messages to an application which interprets the command and programs each **dds!** using the SPI interface. A glossary of the commands used is presented in Appendix ???. Once the **dds!** has been updated, the the command is triggered to start using a digital signal so that the time at which the frequency updates is synchronised with the other hardware.

1.4 Controlling the MOTs

Effective trapping and cooling of Rubidium requires careful control of the light and magnetic fields used to create the **mot!**. Firstly, it is necessary to ensure the **mot!** beams are well polarised, with equal intensities at the centre of the trap. Otherwise, the imbalance of radiation pressure from each beam can exert a net force on the atoms, which causes the **mot!** to form at a position where the magnetic field is not zero [Steane1992]. When this field is switched off prior to cooling in an optical molasses, this force will push the atom cloud away from the equilibrium position and likely prevent further cooling. A similar argument holds in the case of balanced intensities and a stray magnetic field, which displaces the **mot!** from the centre of the beams to a position where the intensities are imbalanced. What follows is a description of the hardware used to provide more precise control of the relative power in each **mot!** beam, as well as the magnetic fields.

1.4.1 Optical Fibre Network

A network of fibre-based beam-splitters and **aoms!s** (**aoms!s**) is used to distribute the light from the μ Quans fibre to each of the beams required for the 2D and 3D **mots!s**. This also provides a means of separate control of the power and frequency of the light

at each output of the fibre network. A diagram of this setup is shown in Figure ???. The fibres are spliced together to minimise insertion loss and improve the alignment of the slow axes of connected fibres. Prior to this, the fibres were connected using mating sleeves, which resulted in polarisation drifts that severely impacted on the stability of the **mots**!s. A set of *Gooch and Housego* fibre **aoms**!s with a central modulation frequency are of 135 MHz are used to individually control the frequency and power of each output. The polarisation of the output from this fibre is purified using a polarising beam-splitter before a **hwp**! aligns the polarisation axis of the light with the slow axis of a **pm**! fibre. The light is first divided on a 1:2 beam-splitter, with 66% exiting one port, used for the 3D **mot**!. The 34% on the other port is then split again using another 1:2 beam-splitter so that 95% and 5% of the power exits each port to provide light for the 2D **mot**! and push beam, respectively.

The light for the 3D **mot**! is spilt using a 1:3 splitter into pairs of outputs for the light along the \vec{x} , \vec{y} and \vec{z} axes. Unlike the outputs along the other axes, the ones used for light along the \vec{z} axis have separate **aoms**!s. This is done so that during the experiment, a single beam along the \vec{z} axis can be used to blow away background atoms (see Section ??? for more details).

1.4.2 Magnetic Field Control

At different stages during the experiment, it is necessary to create a magnetic field to polarise the atoms along different axes. For this reason, the bias coils are all controlled using a bipolar current driver, where the output current is proportional to a control voltage. This control voltage is input at the non-inverting terminal of an OPA549 op-amp. The coils are placed in series with a sense resistor of resistance R_s at the output. The circuit is configured so that the voltage at the inverting terminal is $V_- = iR_s$. This forms a negative feedback loop, so that if the output current drops due to ohmic

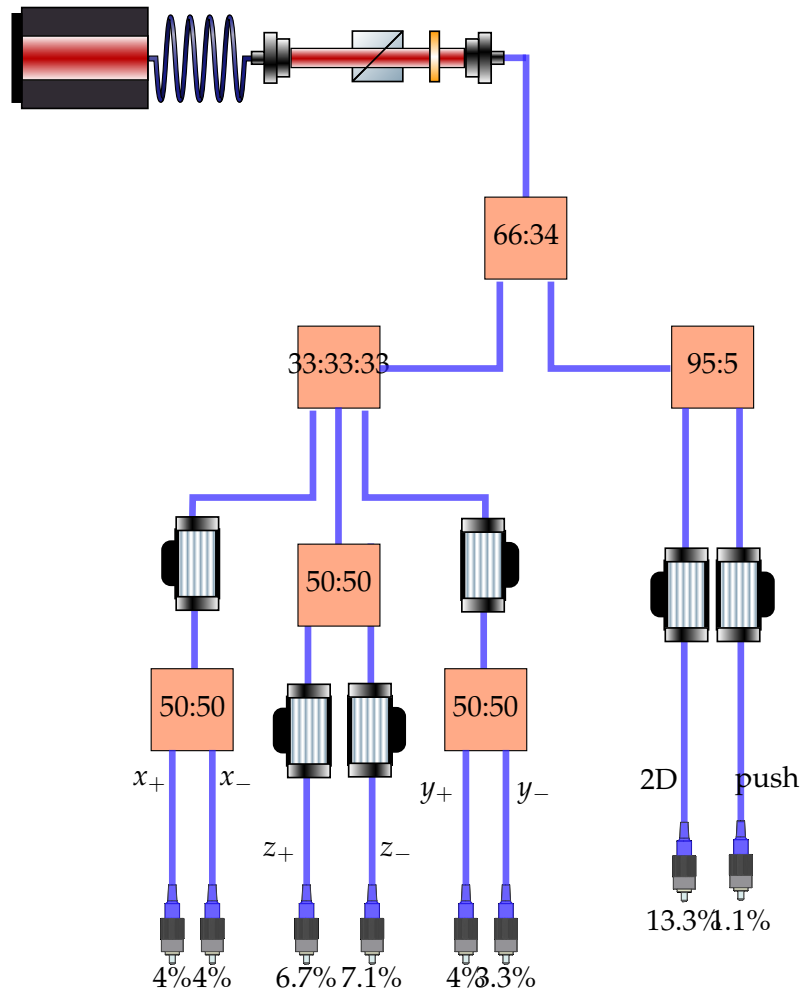


Figure 1.13: Fibre splitter and aoms for MOT light distribution. The polarisation of the cooling and repump light from the μ Quans laser is aligned to the fibre network using a **pbs** and **hwp**. Apart from the outputs for the \vec{x} and \vec{y} 3D **mot** beams, which have a single **aom** per axis, the power and frequency at each output can be controlled independently. The percentages shown are the relative power at each output, accounting for insertion loss and driving each **aom** with the optimum RF power.

heating of the coils, the op-amp increases the output voltage to keep the voltage at the two input terminals equal. The bias coils can be supplied with up to 1 A using a control voltage of 10 V.

This same circuit is used to control the 3D **mot!** coils, except for the fact that their larger resistance necessitates a larger gain to achieve the current necessary to produce a strong field gradient. During the experiment, the 3D **mot!** coils need to be switched off rapidly, to allow for effective sub-Doppler cooling of the atoms. Since the coils act as an inductive load, the time taken for the current is determined by the time constant $\tau = L/R$. However, if a negative voltage is applied, the energy stored in the inductor (and hence, magnetic field) will dissipate at a faster rate. To determine the minimum time taken for the field to switch off, a flux-gate magnetometer was used to measure the time taken for the magnetic field outside the chamber to reach a steady value after changing the voltage across the coils. With an applied voltage of 0 V, a $1/e$ decay time of 2.5 ms. Under the maximum voltage of -24 V that the current driver can output, the field can be completely switched off in $800\text{ }\mu\text{s}$.

The quadrupole coils for the 2D **mot!** are controlled in a different manner. They are switched off using an IGBT to cut the flow of current when the gate voltage drops below a threshold value. This generates a large back-EMF that opposes the changing current. To prevent damage to the transistor, a diode and $10\text{ }\Omega$ power resistor are placed in parallel with the coils. This allows the current generated by the back-EMF to dissipate without damaging the IGBT. These field from these coils can be switched off in less than 1 ms, but this is less critical than the time taken for the 3D **mot!** quadrupole field to switch off.

2D MOT				3D MOT			
Laser Power		Magnetic Field		Laser Power		Magnetic Field	
Cooling	60 mW	$d\vec{B}/d\rho$	18 G cm^{-1}	Cooling	130 mW	$d\vec{B}/dz$	15 G cm^{-1}
Repump	6 mW	B_x	0.48 G	Repump	13 mW	B_x	1 G
Push	500 μW	B_y	-0.46 G			B_y	-0.5 G
						B_z	0.22 G

Table 1.2: Typical optical and magnetic parameters used for the 2D and 3D **mots!**s. The optical powers listed are the total used for each **mot!**, which is divided into separate beams. The bias field strengths are the values used during the preliminary trapping stage of the experiment. The specified field gradients are given along the radial direction and the symmetry axis of the quadrupole coils for the 2D and 3D **mots!**s, respectively.

1.5 Characterising the MOTs

This section discusses the performance of the 2D and 3D **mots!**s for trapping and cooling **rb87!**. The main goal of this stage of the experiment is to quickly produce an ensemble of trapped, cold atoms in the 3D **mot!**. For this reason, the loading rate of the 3D **mot!** is a useful figure-of-merit. As further cooling in an optical molasses is necessary to achieve a sufficiently cold ensemble for interferometry (see Section ??), the temperature of atoms in the **mot!** will not be discussed in detail.

At the start of the experiment, the light and magnetic fields to produce the 2D and 3D **mots!**s are switched on. Table ?? shows the typical values for the cooling and repump power, as well as the field gradients and bias fields used. The cooling light is detuned by -2Γ from the $|F = 2\rangle \rightarrow |F' = 3\rangle$ transition for the 2D **mot!** and -2.5Γ for the 3D **mot!**, whereas the push beam is at resonance. The light and magnetic fields for the 2D **mot!** are switched off after 100 ms and the 3D **mot!** is kept on for a further 50 ms to allow for the transit of the remaining atoms from the 2D **mot!** to the 3D **mot!**. After a sufficient number of atoms are loaded, the experiment proceeds by switching off the 3D quadrupole field prior to cooling in an optical molasses.

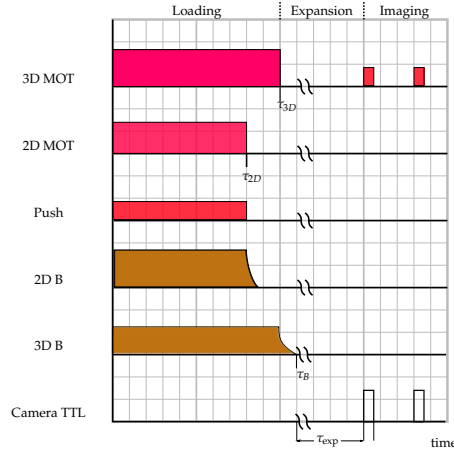


Figure 1.14

1.5.1 3D mot! Loading Rate

The loading rate of the 3D **mot!** from a beam of atoms originating from the 2D **mot!** can be understood using the following rate equation

$$\frac{dN}{dt} = R\phi_{rb} - (\alpha\phi_{rb} + \beta n_{bg}) N - \gamma N^2 \quad (1.3)$$

where ϕ_{rb} is the flux of rubidium through 3D **mot!** capture volume and R describes the rate at which rubidium is cooled and trapped such that $R\phi_{rb}$ is the loading rate of the 3D **mot!**. The second term describes a loss rate due to collisions between trapped atoms and untrapped rubidium and background atoms. These loss rates are parameterised by α and β , respectively. The final term describes the loss of atoms from the trap due to intra-trap collisions [Prentiss1988] which depends on the density of atoms in the trap. In the case of a large flux of atoms from the 2D **mot!** the first two terms dominate, leading to a simple solution for the number of atoms in the 3D **mot!**

$$N(t) = \frac{R\phi_{rb} \left(1 - e^{-t(\beta n_{bg} + \alpha\phi_{rb})}\right)}{\beta n_{bg} + \alpha\phi_{rb}} \quad (1.4)$$

which has a steady-state atom number given by

$$N_{\infty} = \frac{R\phi_{rb}}{\beta n_{bg} + \alpha\phi_{rb}} \quad (1.5)$$

Under a small atomic flux, both the loading rate and steady-state atom number increase as the flux of atoms from the 2D **mot!** increases. Once this flux is great enough, the loss due to background atom collisions is small compared to the loss due to rubidium collisions and the final number is independent of ϕ_{rb} .

To optimise the 3D **mot!** loading rate, we varied both the . The flux of atoms from the 2D **mot!** depends on the 2D **mot!** loading rate, which in turn depends on the capture volume and rubidium number density inside the cell. Without any longitudinal cooling, a significant fraction of atoms leaving the cell will have a velocity greater than the 3D **mot!** capture velocity [Schoser2002].

The effect of varying the partial pressure of rubidium inside the source cell are shown in Figure ?? . For a range of dispenser currents, the number of atoms as a function of loading time was measured. At low partial pressures, the loading rate increases due to the increase in the flux from the 2D **mot!**. As the pressure increases, the increasing flux gives a larger steady-state number of atoms, up until the background pressure becomes negligible. Figure ?? and Figure ?? compare the loading curves observed with and without the push beam. Below a threshold pressure, the push beam greatly improves the loading rate since a greater fraction of the atoms can be captured in the 3D **mot!**. Figure ?? shows the fitted loading rate for each scenario and indicates a clear optimum pressure, where the loading rate is maximised and the same steady-state atom number is reached with or without the push beam. Above this pressure, the loading rate is sharply reduced as the increased collision rate between cold atoms from the 2D **mot!** and hot untrapped ones reduces the atomic flux. This also increases the mean velocity of atoms in the beam, since faster ones are less likely to collide with a

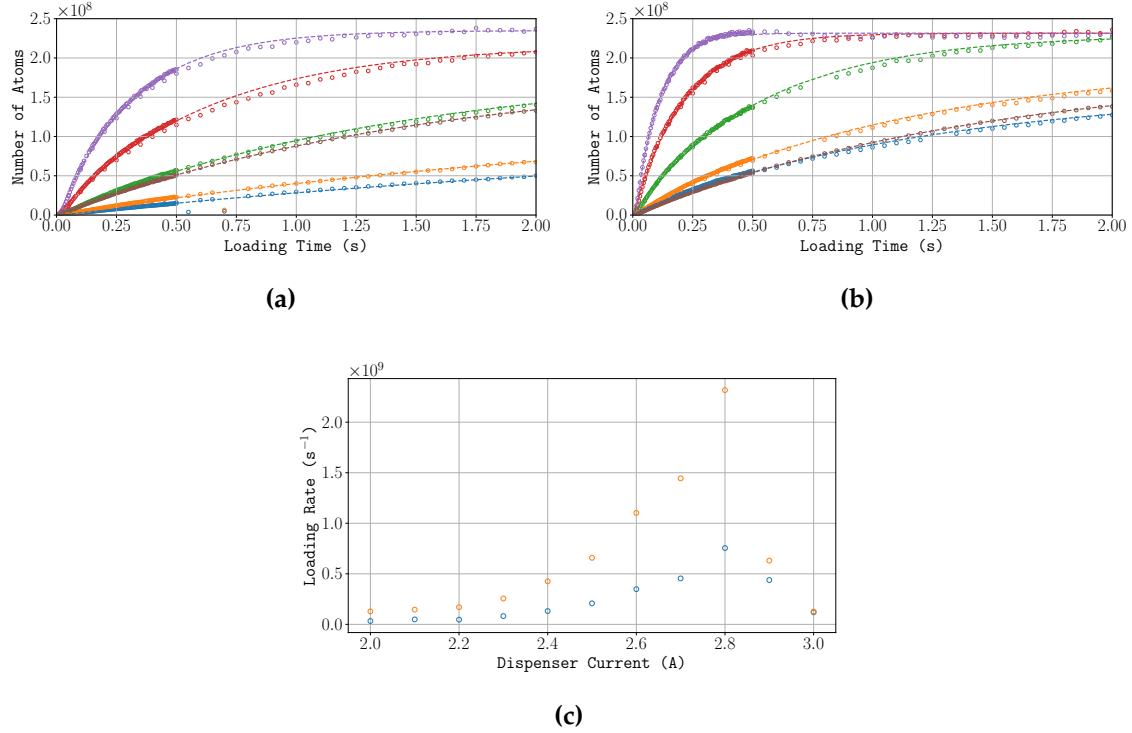


Figure 1.15: Number of atoms in the 3D **mot!** over time for a range of dispenser currents. For clarity, only the loading curves for dispenser currents of 2 A (blue), 2.2 A (orange), 2.4 A (green), 2.6 A (red), 2.8 A (purple) and 3 A (brown) are shown in (a) and (b), which present the number of atoms over time without and with a push beam, respectively. The loading rate ($R\phi_{rb}$ in equation (??)) in both instances is shown in (c). As the partial pressure of rubidium increases, the flux of atoms from the source cell increases. By longitudinally cooling the atoms, the push beam enhances the loading rate of the 3D **mot!**. Above a dispenser current of 2.8 A, the collision rate with hot untrapped atoms greatly reduces the atom flux, reducing both the loading rate and steady-state atom number.

background atom before exiting the cell. At very high pressures, the mean velocity is so great that only a small fraction of atoms can be captured and the push beam has little effect on the loading rate.

1.6 Conclusion

This chapter has introduced the components of the experiment that were used to trap and cool atoms in a **mot!**. This is used to prepare an ensemble of cold atoms in a pure quantum state, suitable for interferometry. An optimisation of the loading rate of the 3D **mot!** was carried out to reduce the dead time between consecutive measurements of acceleration using the interferometer.

